IEEE Access
Multidisciplinary | Rapid Review | Open Access Journal

Received October 1, 2018, accepted October 15, 2018, date of publication November 1, 2018,
date of current version November 19, 2018.

Digital Object Identifier 10.1109/ACCESS.2018.2877745

A Novel Broadband Bi-Functional Metasurface for Vortex Generation and Simultaneous RCS Reduction

KAI-YUE LIU, WEN-LONG GUO, GUANG-MING WANG, (Member, IEEE), HAI-PENG LI, AND GANG LIU
Air Force Engineering University, Xi'an 710051, China
Corresponding author: Guang-Ming Wang (wgming01@sina.com)

This work was supported in part by the National Natural Science Foundation of China under Grant 61871394.

ABSTRACT In this paper, a broadband bi-functional metasurface is presented with capabilities of generating vortex beam for y-polarization and reducing the backward radar cross section (RCS) for x-polarization. With careful optimization, a meta-atom is first designed to control reflection phases for orthogonally polarized wave independently. Then, an integrated phase profile is employed to convert y-polarized spherical wavefront into a vortex spiral one, shaping a vortex high gain beam in the far-field region. By arranging a checkerboard-like phase profile onto the surface for x-polarization, the reflected wave in the backward direction will be canceled, consequently leading to the backward RCS reduction for x-polarization. Combining the above-mentioned cases into a whole, a compact bi-functional metasurface is designed, simulated, physically implemented, and finally measured. In good agreement with the simulated results, the measured ones show that the RCS reduction of 10 dB for x-polarization in comparison with a same-sized metallic plate can be realized over a 67.7 % frequency bandwidth (9–18.2 GHz). Besides, high-efficiency vortex beam conversion effect for y-polarization over a broad range of 11.2–18.2 GHz (47.6%) can also be observed from the measured results.

INDEX TERMS Metasurface, bi-functional, vortex beam generator, RCS reduction.

I. INTRODUCTION

Metasurface (MS), namely the 2D equivalent of metamaterial, has always been a research hotspot since it was first proposed by Yu [1] in 2011. Generally, by introducing a series of subwavelength quasi-periodic meta-atoms on the interface, some certain electronic or magnetic resonances will be introduced, resulting in an abrupt phase change or polarization rotation or even an amplitude change in reflection or refraction mode, thus finally forming a so-called MS with ability of flexibly manipulating electromagnetic (EM) wave [2]–[8]. And till now, numerous intriguing applications of MSs, such as flat lens [2], [4], vortex beam generator [9], [10], invisible cloak [11] and holographic imagers [12], have been successfully implemented and partially applied in real world. Among them, the vortex beam generator and invisible cloak are relatively more fascinating by virtue of their potential in enhancing data capacity in communication system and remarkably reducing the RCS in radar system.

Vortex beam, with spiral phase front carrying orbital angular momentum (OAM), has been proved to be a validate solution to increase the channel capability, thus may being selected to solve the problem of limited spectrum and polarization resources. To generate vortex beams, various approaches are adopted. For example, spiral phase plates [13], subwavelength gratings [14], antenna arrays [15], and computer generated holograms [16] were typically employed in the past. But the recently proposed MS is increasingly becoming the most promising alternative to generate vortex beams owing to its unprecedented capability of modifying wavefront of EM wave [9], [10]. Moreover, the low loss and thin structures of MS allowing bulky components to be shrunk down to planar device makes MSs more competitive in generating vortex waves. Nevertheless, it's still a challenge to design a broadband vortex generating MS, especially with ability of RCS reduction at the same time.

For the invisible cloak application in microwave frequency domain, a simple but efficient method to reduce RCS of a

target by using MS is to put a random or a certain phase profile onto the surface so as to redirect the scattering fields. In this way, scattering cancellation [17], [18] and diffusion-like scattering [19], [20] are the two common methods employed in practical design. Based on those techniques, variable works focusing on RCS reduction in a broad frequency band have been successfully realized and published to date. However, with integrated and compact development of electronic devices, a MS device with a bare function of RCS reduction is gradually unable to meet the requirement. Therefore, to design a low RCS characteristic surface with capability of generating vortex beam seems to be more fascinating and dramatically in demand.

In this paper, we focus on designing a bi-functional MS to simultaneously generate vortex beam and reduce the backward RCS. Specifically, a compact anisotropic meta-atom is firstly optimized with reflection phases independently controlled upon x-and y-polarized incident EM wave. Then an integrated phase profile is utilized to convert the y-polarized spherical wavefront into a vortex spiral counterpart, while a checkerboard-like phase profile is employed to destroy the plane wavefront of x-polarized incidence so as to reduce the backward RCS for x-polarization. Experimental results coincide well with the simulated ones, indicating a relative 67.7% 10-dB RCS reduction bandwidth (9 GHz to 18.2 GHz) for x-polarized incidence and a high-efficiency vortex beam conversion for y-polarization over a broad range of 11.2 – 18.2 GHz. With beam shaping for y-polarization and scattering cancellation for x-polarization, the proposed bi-functional MS offers an alternative to design multi-functional devices, which may have great potential applications in wireless communications or radar detection systems.

In what follows, the bi-functional MS will be theoretically analyzed in part II and then be carefully designed in part III. Numerical and experimental results are finally demonstrated in part IV to validate our theoretical prediction.

II. THEORY ANALYSIS

To begin with, the operating mechanism for the bi-functional MS will be firstly introduced. Notably, the key points of designing bi-functional MS here are to optimize a meta-atom independently responding for orthogonally polarized wave, and then to set different phase profiles for orthogonal polarizations, so as to achieve different functions for differently polarized wave. The carefully designed meta-atom will be introduced in the part of model design, while the two functions of orthogonally polarized wave will be presented as follow.

A. SCATTERING CANCELLATION FOR X-POL.

Scattering cancellation is typically realized by employing two elements with phase difference of 180° distributed as a checkerboard-like alternant pattern, finally forming a beam null in the backward direction. Previously, researchers tend to design a meta-atom with reflection phase of 0° which is also called artificial magnetic conductor (AMC) [18], [21], in order to design a scattering cancellation surface by combining PEC and AMC. But in this way the backward RCS reduction bandwidth is always limited. Afterwards to broaden the operating bandwidth, researchers are inclined to use two elements with phase difference of 180° instead of PEC and AMC [22]. Besides, the array factor is always adopted to analyze and predict the performance of the designed scattering cancellation surface, which can be described as

$$AF = I_0 \sum_{m=1}^{M} e^{j(m-1)(kd_x \sin\theta \cos\varphi + \beta_x)} \cdot \sum_{n=1}^{N} e^{j(n-1)(kd_y \sin\theta \sin\varphi + \beta_y)} \quad (1)$$

where dx and dy are the spacings between the elements along x and y axis, while β_x and β_y represent the progressive phase shifts between the elements in x and y directions. Besides, the parameters of M and N are the number of elements in x and y directions. Based on the array factor analysis, the principal scattering direction can be found from

$$\tan\varphi_0 = \frac{\beta_y d_x}{\beta_x d_y} \quad (2)$$

$$\sin^2\theta_0 = (\frac{\beta_x}{kd_x})^2 + (\frac{\beta_y}{kd_y})^2 \quad (3)$$

where (θ_0, φ_0) is the maximum scattering direction. Moreover, in comparison with a same-sized metal plane, the RCS reduction level of the scattering surface in the backward direction can be derived as

$$R - RCS = 10\log(\frac{A_1 e^{jP_1} + A_2 e^{jP_2}}{2}) \quad (4)$$

in which the abbreviation of *R-RCS* shows the RCS reduction level. A_1 and A_2 are the reflection coefficients whereas P_1 and P_2 represent the reflection phases for the two designed elements. Usually backed by a metal pattern to ensure entire reflection, the two elements are both with a reflection coefficient equal to 1. Then calculated from Eq. (4), the bandwidth of 10 dB RCS reduction is equivalent to the bandwidth of

$$180° - 37° \le |P_1 - P_2| \le 180° + 37° \quad (5)$$

Unambiguously, in order to cancel the backward scattering for x-polarization, two elements should be first optimized with phase difference for x-polarization fluctuating from 143° to 217° in a relatively broad bandwidth.

B. VORTEX BEAM GENERATING FOR Y-POL

The principle of generating vortex beam is to introduce azimuthal phase dependence $e^{-jl\varphi}$ into the wave. MS with spiral phase profile as depicted in Eq. (6) has been proved to be a validate method to generate vortex beam carrying OAM. But the described scenario only happens when the MS is impinged by plane-wave, which is easily obtained in optical spectrum. Notably, it is much easier to generate spherical wave than plane wave in microwave frequency domain.

Therefore, a phase plate operating in microwave frequency band to convert spherical wave into plane wave is critically in demand. Fortunately, a MS with hyperbolical phase profile as shown in Eq. (7), namely focusing MS, is capable of focusing plane wave to a focal spot and conversely converting spherical wave emitted from the focal spot into plane wave [23], [24]. In order to generate vortex beam from a point source, the ultrathin flat MS should incorporate the two distinct phase profiles: focusing and vortex, so that the secondary wave emerging from the MS can constructively interfere to produce a vortex beam with specific topological charge. With this method, the integrated phase profile to generate vortex beam from a spot source should abide by the form of Eq. (8).

$$\Phi_1(x, y) = l \tan^{-1}(y/x) \tag{6}$$

$$\Phi_2(x, y) = \frac{2\pi}{\lambda}\left(\sqrt{x^2 + y^2 + F^2} - F\right) \tag{7}$$

$$\Phi(x, y) = \frac{2\pi}{\lambda}\left(\sqrt{x^2 + y^2 + F^2} - F\right) + l \tan^{-1}(y/x) \tag{8}$$

Furthermore, the array factor can also be employed to predict the far-field performance of the vortex beam generator. Typically, for a concentric ring array with discrete vortex phase distribution, the array factor can be described as [25]

$$AF \approx \sum_{m=1}^{M} N_m j^{-l} e^{jl\varphi} J_l(kr_m \sin\theta) \tag{9}$$

where r_m represents the radius of m-th ring while N_m is the number of elements in m-th ring. J is the Bessel function and l represents the topological charge. Obviously, a beam null will appear at the direction of $\theta = 0°$ when l is set to be a non-zero constant. Besides, the principal radiation maximum can also be figured out when the aperture diameter and the topological charge are provided first. To be noted, this prediction also works when the array configuration changes from a circle to a square, especially when the aperture size is large enough. In a word, to generate a vortex beam from a point source for y-polarization as shown in Fig. 2, an integrated phase profile calculated from Eq. (8) should be imposed on the surface, which will finally result in a vortex beam carrying OAM with far-field pattern predicted by Eq. (9).

III. MODEL DESIGN

Based on abovementioned analysis, an anisotropic meta-atom with capability of controlling orthogonally polarized waves independently is urgently in demand, so that the above proposed phase profiles can be imposed on the surface simultaneously.

A. DESIGN OF ANISOTROPIC META-ATOM

Cross-shaped meta-atom has been proved to be an effective element [26] to manipulate orthogonally polarized wave independently. However, due to its single electric resonance, the coverage of reflection phase of traditional cross-shaped element cannot cover 360° which limits the operating bandwidth severely. By using meandering strip line, multi-resonant is introduced, and cross-shaped element with meandering strip line can increase reflection phase of element dramatically, so as to broaden operation bandwidth. Here, by introducing meandering strip line into cross-shaped element, a novel meta-atom is devised as shown in Fig. 3, with ability of independently controlling orthogonally polarized waves. As depicted in Fig. 3 (a), the crossed meandering pattern is etched on a substrate backed by a metallic ground, with geometric dimensions of $p = 6.8$ mm, $h = 3$ mm, $d = 0.2$ mm. Copper thin film with a thickness of 0.036 mm is used to form the top metallic pattern and the ground plane, while the dielectric layer is with relative permittivity of 2.65 and loss tangent of 0.009. To figure out the resonant mechanism of the element, the reflection phase spectra and surface current are simulated at resonant frequency with

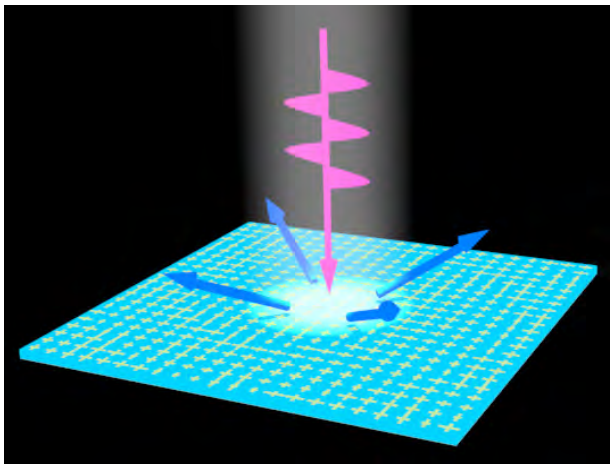

FIGURE 1. Schematic diagram of RCS reduction for x-polarization. The incident plane wave (red arrow) is split into four lobes (blue arrows) so as to reduce the backward RCS.

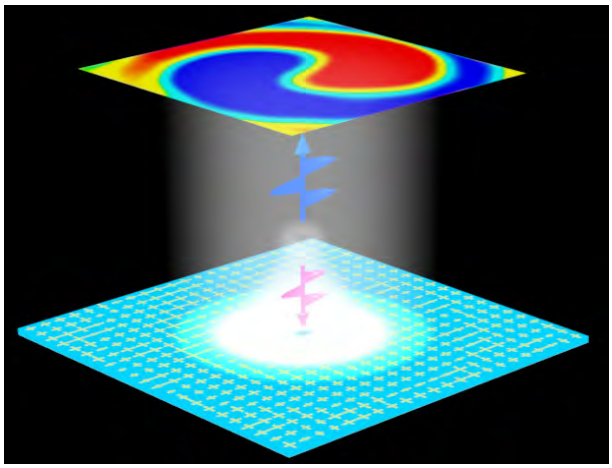

FIGURE 2. Schematic diagram of vortex beam generating for y-polarization. The incident spherical wave as represented by the red arrow is finally engineered to form a vortex beam in reflection mode as depicted by the blue arrow.

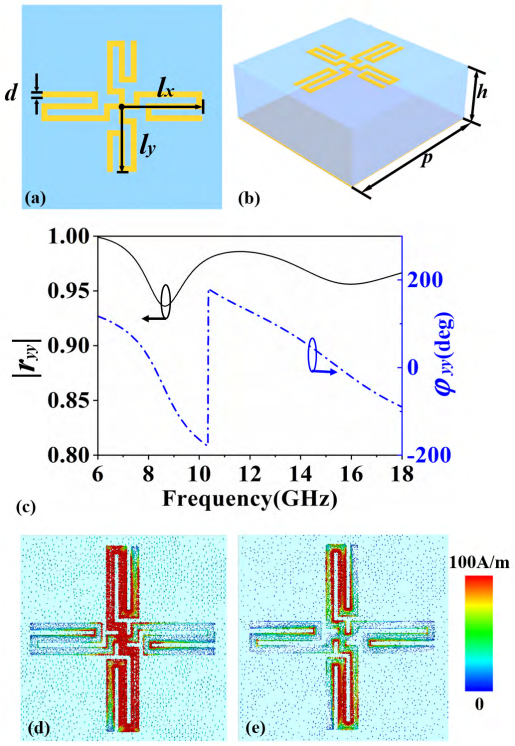

FIGURE 3. Topology of proposed meta-atom, simulated flection spectra and surface current at resonant frequency. (a) Top view and (b) perspective view of meta-atom; (c) simulated spectra of reflection coefficient and phase; surface current of meta-atom at (d) $f_1 = 8.2$GHz and (e) $f_2 = 15.5$GHz.

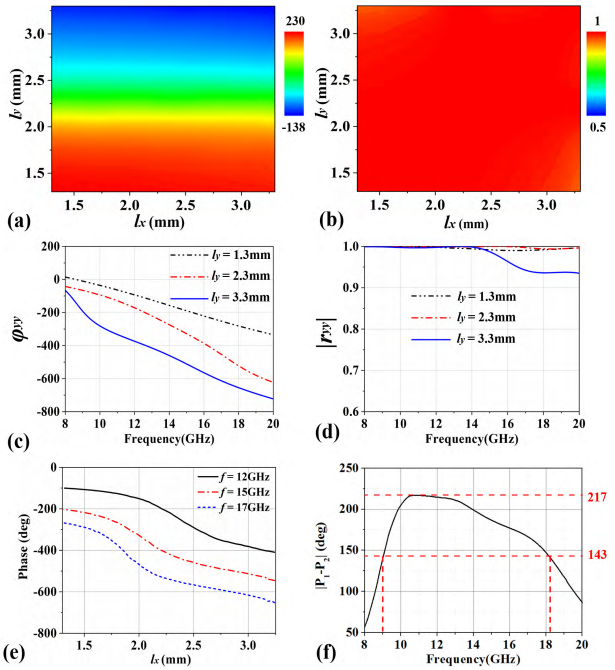

FIGURE 4. (a) and (b) depict the reflection phase and amplitude for y-polarization varying with l_x and l_y at 15GHz. (c) and (d) plot the reflection phase and amplitude for y-polarization in the 8-20GHz frequency range (e) The reflection phase for x-polarization varying with l_x at different frequencies. (f) The phase difference between the two meta-atoms with $l_x = 2.3$ mm and 3.2 mm.

$l_x = l_y = 3.3$ mm. As plotted in Fig. 3(c), dual resonance appears in about $f_1 = 8.2$GHz and $f_2 = 15.5$GHz, which plays an important role in extending phase variation range. From the surface current, the resonance between the first two bars, middle "" and the ground plane explains the resonance f_1, while the resonance between middle bar and ground plane explains the resonance f_2. To illustrate the independent controls of orthogonal polarizations, Fig. 4(a) and (b) show the maps of reflectivity and reflection phase of y-polarization with l_x and l_y both varying from 1.3 mm to 3.3 mm. Obviously, the y-polarized incident wave is almost totally reflected, and the reflection phase only varies with l_y. That is to say, reflection phase of y-polarization is only dependent on l_y but immune to l_x. Similarly, the same conclusion can be drawn that the reflection phase of x-polarization relies on l_x but is immune to l_y. In a word, reflection phases for x- and y-polarization are independently controlled by parameters of l_x and l_y. Besides, to figure out the broadband properties of the meta-atom, the reflection phase and reflectivity of y-polarization under the condition of a fixed l_x at 2 mm and variable l_y, as depicted in Fig. 4(c) and (d). One can observe that reflection phase cover range reaches 360° in a broad bandwidth with the variation of l_y and reflectivity $|r_{yy}|$ are above 0.93. Fig. 4(e) depicts the reflection phase for x-polarization varying with l_x at different frequencies. The phase lines of different frequencies are near parallel to each other, illustrating broad operating bandwidth of the finally engineered MS.

To fulfil scattering cancelling for x-polarization, as shown in Fig. 4(f) two elements with l_x equal to 2.3 mm and 3.2 mm are selected to configurate the surface with checkerboard-like phase profile. Obviously, the phase difference fluctuates from 143° to 217° in 9 – 18.2 GHz, which will correspondingly lead to the backward RCS reduction of 10 dB in the bandwidth of 9 -18.2GHz according to Eq. (5). For point source, incidence angles vary with positions of elements, so phase curves of the meta-atom for oblique incidence should be taken into consideration. As plotted in Fig. 5, the reflection phase only fluctuates within 40° from 8GHz to 18GHz when the incident angle varies from 0° to 30°, which can be neglected in our design.

B. CONFIGURATION OF BI-FUNCTIONAL MS

The designing process of configurating bi-functional MS is to assemble anisotropic meta-atoms to fulfil different phase distributions for orthogonally polarized waves. With this in mind, we show the checkerboard-like phase profile for x-polarization in Fig. 6(a) to cancel the backward reflection, and in Fig. 7(b) we depict the corresponding MS configuration by modulating parameter l_x. Similarly, calculating from Eq. (8) we show the integrated phase profile for y-polarization in Fig. 6(b) to generate vortex beam, and in Fig. 7(c) we depict the according MS configuration by

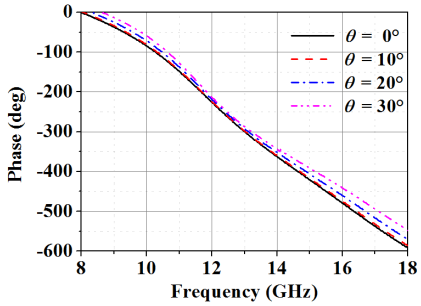

FIGURE 5. The reflection phase of the meta-atom with different oblique incident angles.

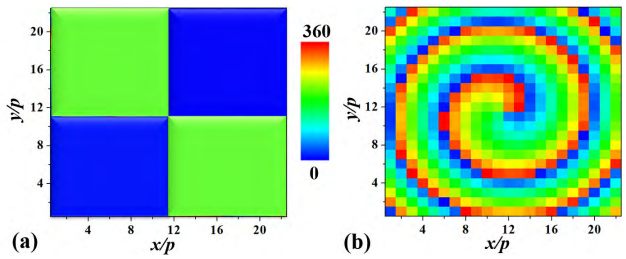

FIGURE 6. Phase profiles for orthogonally polarized wave. (a) x-polarization. (b) y-polarization.

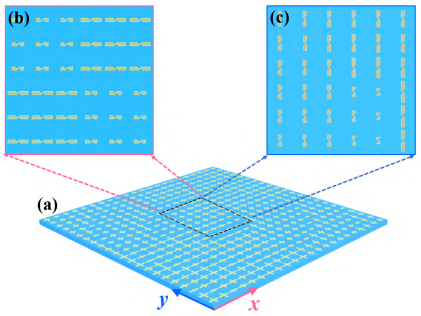

FIGURE 7. The designed MS prototype. (a) The finally engineered MS. (b) and (c) depict the concrete structures for x- and y-polarization.

adjusting the parameter of l_y. To be noted, the focal distance is fixed for 60mm and the topological charge is set for 1. As shown in Fig. 7(a), the finally assembled sample consists of 22 × 22 elements and thus occupies a size of 149.6 × 149.6 mm^2. In what follows, the designed MS will be illuminated by x-polarized plane wave to investigate its scattering characteristic, and then will be impinged by spherical wave emitted from the focal spot to generate vortex beam carrying OAM.

IV. NUMERICAL AND EXPERIMENTAL RESULTS

A. SCATTERING CANCELLATION FOR X-POL

With x-polarized plane wave impinging on the surface, the configurated MS prototype is firstly simulated by using a FDTD method. Fig. 8(a) illustrates the simulated three-dimensional scattering pattern under x-polarized normal incidence. Consistent with the theoretical prediction, the

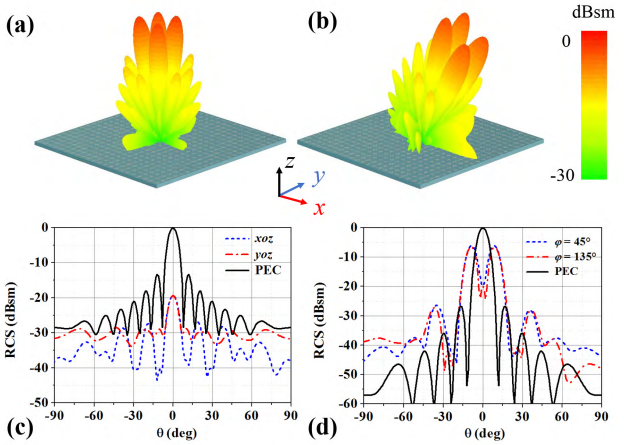

FIGURE 8. (a) and (b) depict three-dimensional scattering patterns of the designed MS under normal and oblique incidence at 15GHz respectively. (c) Normalized two-dimensional scattering patterns on the planes of $\varphi = 0°$ and $\varphi = 90°$ at 15GHz. (d) Normalized two-dimensional scattering patterns on the planes of $\varphi = 45°$ and $\varphi = 135°$ at 15GHz.

incident plane wave is split into four beams with reflected lobes appearing at $\varphi = 45°$, 135°, 225° and 315°, which correspondingly reduces the normal reflection dramatically and finally leads to a considerable backward RCS reduction. Besides, Fig. 8(b) shows the reflection pattern under oblique incidence, which unanimously demonstrates that the specular reflection of the MS for oblique incidence is still relatively small. To quantitatively analyze the performance of RCS reduction, two-dimensional scattering patterns of 15GHz on *xoz*and *yoz* planes are plotted in Fig. 8(c). Clearly, the RCS in backward direction is considerably suppressed (20dB lower than PEC) in comparison with a same-sized metallic plate. Fig. 8(d) shows the scattered fields versus the elevation angle theta (θ) at 15GHz along the diagonal planes. The maxima of the RCS are located at $\theta = 9°$, which coincide well with the angle predicted by Eq. (2) and Eq. (3). Furthermore, the maximum RCS of the checkerboard surface is 6.2 dB less than that of the same-sized metallic plate, which is because the reflected fields are redirected into four main beams, instead of the single main lobe of the metal plane. Finally, as shown in Fig. 9 the MS prototype is fabricated and then measured in an anechoic chamber to minimize the reflection from surroundings as well as to avoid the unwanted effects from the environment. Fig. 10(a) shows the experimental and numerical backward RCS reduction of the designed MS compared with a same-sized metallic plate under normal incidence. Comparison of the measured and the simulated RCS reduction of 10dB results in an excellent agreement over the frequency band of 9 -18.2GHz (67.7%). Fig. 10(b) and Table 1 are all employed to illustrate the 10-dB reduction bandwidth of backward RCS changing with incident angles. Unambiguously, despite the 10 dB RCS reduction bandwidth narrows when the incident angle increases, we still achieve a 57.2% bandwidth of 10 dB RCS reduction when the prototype is illuminated with incident angle of 40°.

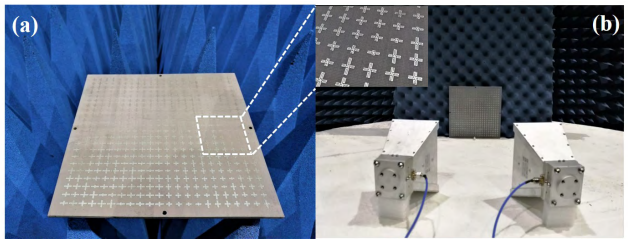

FIGURE 9. (a) Fabricated MS prototype and (b) the measured setup of backward RCS. Inset view depicts the structure details of the MS sample.

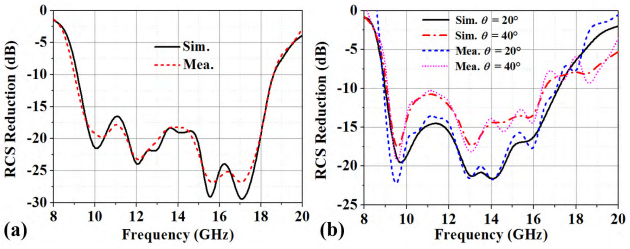

FIGURE 10. Simulated and measured backward RCS reduction compared with a same-sized metal plane under (a) normal and (b) oblique incidence.

TABLE 1. RCS reduction bandwidth of different incident angles.

Incident Angle	10-dB RCS Reduction Bandwidth
0°	67.7%
20°	62.6%
40°	57.2%

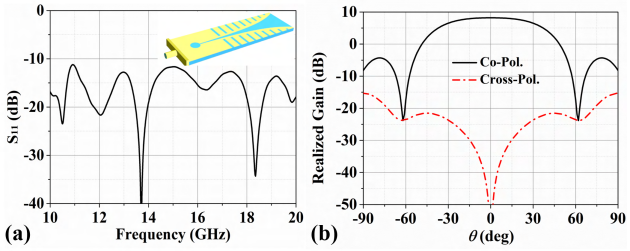

FIGURE 11. Performances of the broadband feed source. (a) Reflection coefficient and (b) two-dimensional far-field pattern on *xoz* plane at 15GHz. Inset is the structure view of the feed.

B. VORTEX BEAM GENERATING FOR Y-POL

As illustrated in the part of theoretical analysis, a broadband point source should be employed to illuminate the designed surface to generate vortex beam carrying OAM. Based on this, a Vivaldi antenna as shown in Fig. 11 is finally selected for the feed source. Fig. 11(a) depicts the feed antenna with impedance matched from 10 GHz to 20 GHz, whereas Fig. 11(b) shows the numerically calculated two-dimensional far-field pattern with a relatively wide beam width and low cross polarization level. The performances exhibited in Fig. 11 (a) and (b) both implies that the Vivaldi antenna

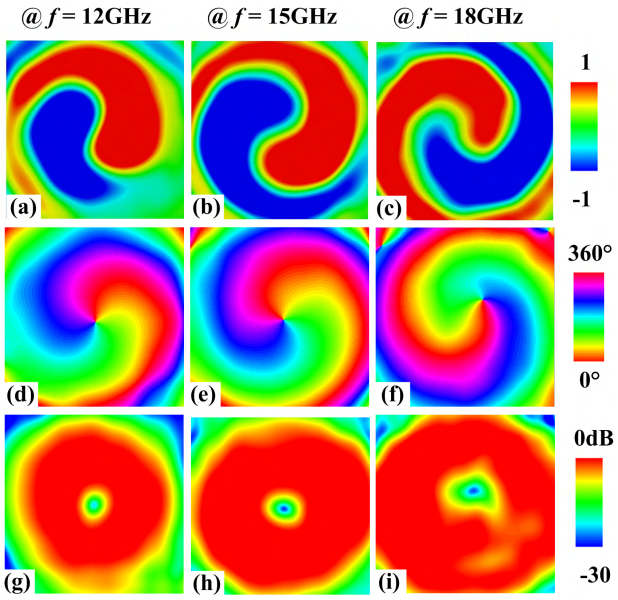

FIGURE 12. Numerical near-field results at (a), (d) (g) 12GHz and (b), (e), (h) 15GHz as well as (c), (f), (i) 18GHz. (a)~(c) represent the real-part of the E-field; (d)~(f) depict the phase of E-field; (g)~(i) are the amplitude of the E-field on the observed plane.

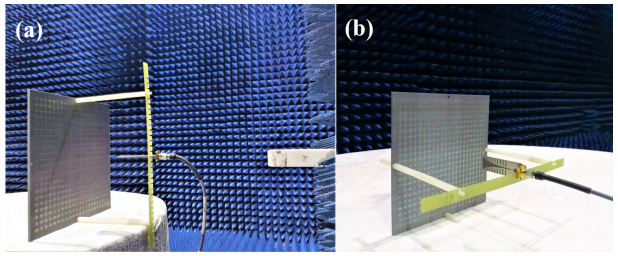

FIGURE 13. Measured setup of MS prototype under y-polarized spherical wave illumination. (a) Far-field and (b) Near-field measurement setup.

is suitable for a broadband spot source emitting spherical wave. By setting the feed antenna at the focal spot of the configurated MS, near-field performances on the observed plane parallel to the MS are numerically calculated and depicted in Fig.12. For convenience and clear identification of the near-field results, all the patterns related to real part and amplitude of E-field at each frequency are normalized to their maximal intensity, and the phase distributions are all converted to the span of 0 ∼ 360. Clearly, the phases shown in Fig. 12 (d), (e) and (f) all exhibit helical wavefront which are consistent with that of the optical vortex beams. Besides, a 360°-phase jump along a full concentric circle further reveals that the helical radio beams have OAM mode of 1. Moreover, as expected in all cases of the amplitude of E-field, the vortex beams exhibit an amplitude null across a wide bandwidth at the central region where the phase and polarization are undetermined due to the vector singularity, thus further revealing the MS's capability of converting *y*-polarized spherical wave into vector-vortex fields. To clarify this further, the fabricated MS prototype is characterized

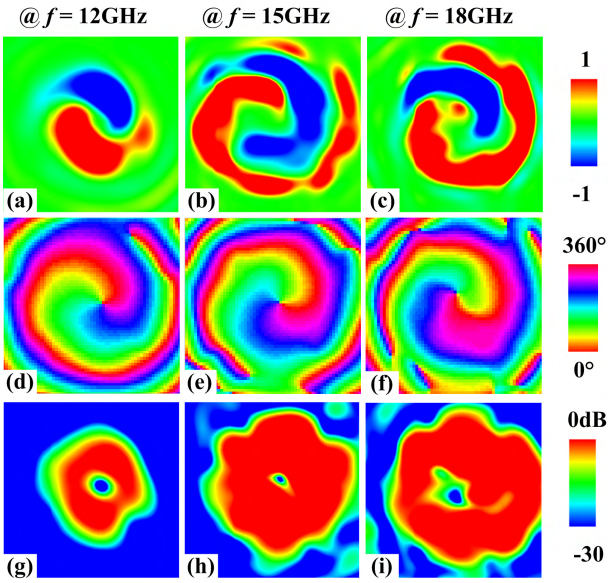

FIGURE 14. Experimental near-field results at (a), (d) (g) 12GHz and (b), (e), (h) 15GHz as well as (c), (f), (i) 18GHz. (a)∼(c) represent the real part of the E-field; (d)∼(f) depict the phase of E-field; (g)∼(i) are the amplitude of the E-field on the measured plane.

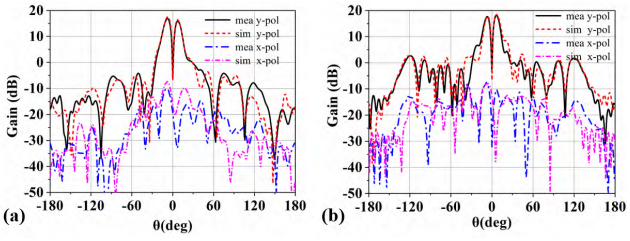

FIGURE 15. Simulated and measured two-dimensional far-field patterns on (a) xoz and (b) yoz plane at the designed frequency of 15GHz.

by the nearfield scanning technique to measure the vortex wavefront in the anechoic chamber as shown in Fig. 13(a). To be noted, far-field characteristics of the assembled sample are also measured. Fig. 13 (b) depicts the far-field testing setup where the distance between prototype and testing probe is larger than $(2D^2)/\lambda$. Here, D represents the aperture size of the prototype and λ is the wavelength at the highest operating frequency. For the convenience of comparison with numerical data, the near-field results depicted in Fig. 14 are all tested on the same plane with numerical setup. It is obvious that the measured data further reveal the vortex characteristic of the generated wave. In addition, the observed region in Fig. 14 seems to be larger and unsatisfactory in comparison with that in Fig. 12. The cause may lay in the fact that the measured plane is slightly larger than the simulated one and the relatively large scanning step in test setup reduces the accuracy. Besides, the machining and measurement errors also deteriorate the testing data. Fig.15 depicts the comparison between the simulated and measured two-dimensional far-field patterns at 15GHz. Obviously confirming with each other, the numerical and experimental data both reveal a

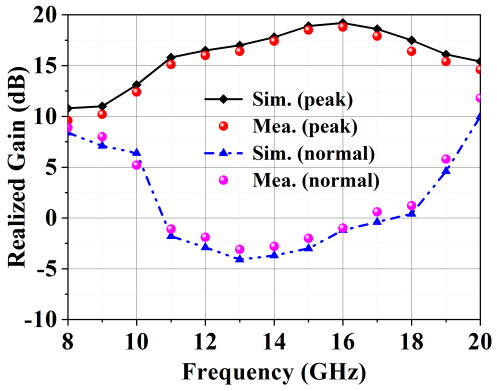

FIGURE 16. Comparation of the realized gain at the maximum and normal reflection. Max. Dir. represents the direction where peak gain is located while Norm. Dir. Is the normal direction.

difference-beam effect on two intersection planes as well as a nulling depth of -23.6dB at the normal direction, thus validating the vortex beam effect with a singularity at the center from far-field patterns. In addition, the peak gain is located at $\theta = 7°$, which coincides with the theoretical prediction of $\theta = 7°$ calculated from Eq. (9). Lastly, to evaluate the bandwidth of vortex beam generator, a simple but efficient method of detecting peak and zero-depth value is adopted. As shown in Fig. 16, we plot the comparison of the realized gain at normal direction and the direction where peak gain is located. With standard of 20 dB difference between the lines of normal direction and peak direction, a bandwidth from 11.2 GHz to 18.2 GHz can be achieved. It must be noted that, the standard proposed here may not be the most efficient way of exhibiting vortex beam conversion efficiency, but it's really simple to assess the operating bandwidth of the generator by combining the near-field results demonstrated in Fig. 15. In a word, the results demonstrate that the MS performs well in generating vortex beam for *y*-polarization over a broad frequency range of 11.2-18.2GHz.

V. CONCLUSION

In conclusion, we propose an anisotropic meta-atom to configurate a bi-functional MS with capability of backward RCS reduction for *x*-polarization and vortex beam generating for *y*-polarization. Performances of the designed bi-functional MS are theoretically predicted, numerically calculated and precisely measured. Coinciding well with the theoretical prediction, simulated and measured results both validate a 67.7% 10-dB RCS reduction bandwidth (9 GHz to 18.2 GHz) for *x*-polarized incidence and a high-efficiency vortex beam conversion for *y*-polarization over a broad range of 11.2 – 18.2 GHz. The present method to devise multi-functional MSs here may pave the way for the integrated and multi-functional development of electronic devices.

ACKNOWLEDGMENT

(Kai-Yue Liu and Wen-Long Guo contributed equally to this work.)

REFERENCES

[1] N. Yu *et al.*, "Light propagation with phase discontinuities: Generalized laws of reflection and refraction," *Science*, vol. 334, no. 6054, pp. 333–337, Oct. 2011.

[2] H.-X. Xu, T. Cai, Y.-Q. Zhuang, Q. Peng, G.-M. Wang, and J.-G. Liang, "Dual-mode transmissive metasurface and its applications in multi-beam transmitarray," *IEEE Trans. Antennas Propag.*, vol. 64, no. 4, pp. 1797–1806, Apr. 2017.

[3] K. Chen *et al.*, "A reconfigurable active huygens' metalens," *Adv. Mater.*, vol. 29, no. 17, p. 1606422, May 2017.

[4] W. Guo, G. Wang, H. Li, T. Li, Q. Ge, and Y. Zhuang, "Design of anisotropic focusing metasurface and its application for high-gain lens antenna," *J. Phys. D, Appl. Phys.*, vol. 50, no. 8, p. 085003, Jan. 2017.

[5] H.-X. Xu *et al.*, "High-efficiency broadband polarization-independent superscatterer using conformal metasurfaces," *Photon. Res.*, vol. 6, no. 8, pp. 782–788, Aug. 2018.

[6] L. Cui *et al.*, "Polarization-dependent bi-functional metasurface for directive radiation and diffusion-like scattering," *AIP Adv.*, vol. 7, no. 11, p. 115214, Nov. 2017.

[7] Y. Zhuang, G. Wang, Q. Zhang, and C. Zhou, "Low-scattering tri-band metasurface using combination of diffusion, absorption and cancellation," *IEEE Access*, vol. 6, pp. 17306–17312, Feb. 2018.

[8] J. R. Cheng and H. Mosallaei, "Optical metasurfaces for beam scanning in space," *Opt. Lett.*, vol. 39, no. 9, pp. 2719–2721, 2014.

[9] H.-X. Xu, H. Liu, X. Ling, Y. Sun, and F. Yuan, "Broadband vortex beam generation using multimode pancharatnam–berry metasurface," *IEEE Trans. Antennas Propag.*, vol. 65, no. 12, pp. 7378–7382, Dec. 2017.

[10] X. Yi *et al.*, "Generation of cylindrical vector vortex beams by two cascaded metasurfaces," *Opt. Express*, vol. 22, no. 14, pp. 17207–17215, Apr. 2014.

[11] P. Su, Y. Zhao, S. Jia, W. Shi, and H. Wang, "An ultra-wideband and polarization-independent metasurface for RCS reduction," *Sci. Rep.*, vol. 6, p. 20387, Feb. 2016.

[12] D. Wen *et al.*, "Helicity multiplexed broadband metasurface holograms," *Nature Commun.*, vol. 6, Sep. 2015, Art. no. 8241.

[13] M. Uchida and A. Tonomura, "Generation of electron beams carrying orbital angular momentum," *Nature*, vol. 464, pp. 737–739, Apr. 2010.

[14] I. R. Srimathi, Y. Li, W. F. Delaney, and E. G. Johnson, "Subwavelength grating based metal-oxide nano-hair structures for optical vortex generation," *Opt. Express*, vol. 23, no. 15, pp. 19056–19065, Jul. 2015.

[15] B. Thidé *et al.*, "Utilization of photon orbital angular momentum in the low-frequency radio domain," *Phys. Rev. Lett.*, vol. 99, no. 8, p. 087701, Aug. 2007.

[16] M. T. Gruneisen, W. A. Miller, R. C. Dymale, and A. M. Sweiti, "Holographic generation of complex fields with spatial light modulators: Application to quantum key distribution," *Appl. Opt.*, vol. 47, no. 4, pp. A32–A42, May 2008.

[17] W. Chen, C. A. Balanis, and C. R. Birtcher, "Checkerboard EBG surfaces for wideband radar cross section reduction," *IEEE Trans. Antennas Propag.*, vol. 63, no. 6, pp. 2636–2645, Jun. 2015.

[18] A. Y. Modi, C. A. Balanis, C. R. Birtcher, and H. N. Shaman, "Novel design of ultrabroadband radar cross section reduction surfaces using artificial magnetic conductors," *IEEE Trans. Antennas Propag.*, vol. 65, no. 10, pp. 5406–5417, Oct. 2017.

[19] K. Chen *et al.*, "Geometric phase coded metasurface: From polarization dependent directive electromagnetic wave scattering to diffusion-like scattering," *Sci. Rep.*, vol. 6, p. 35968, Oct. 2016.

[20] Y. Zhuang, G. Wang, J. Liang, T. Cai, W. Guo, and Q. Zhang, "Flexible and polarization-controllable diffusion metasurface with optical transparency," *J. Phys. D, Appl. Phys.*, vol. 50, no. 46, p. 465102, 2017.

[21] J. C. I. Galarregui, A. T. Pereda, J. L. M. de Falcón, I. Ederra, R. Gonzalo, and P. de Maagt, "Broadband radar cross-section reduction using AMC technology," *IEEE Trans. Antennas Propag.*, vol. 61, no. 12, pp. 6136–6143, Dec. 2013.

[22] Y. Jia, Y. Liu, Y. J. Guo, K. Li, and S.-X. Gong, "Broadband polarization rotation reflective surfaces and their applications to RCS reduction," *IEEE Trans. Antennas Propag.*, vol. 64, no. 1, pp. 179–188, Jan. 2016.

[23] H. Li, G. Wang, H.-X. Xu, T. Cai, and J. Liang, "X-band phase-gradient metasurface for high-gain lens antenna application," *IEEE Trans. Antennas Propag.*, vol. 63, no. 11, pp. 5144–5149, Nov. 2015.

[24] K. Liu, G. Wang, T. Cai, W. Guo, Y. Zhuang, and G. Liu, "Ultra-thin circularly polarized lens antenna based on single-layered transparent metasurface," *Chin. Phys. B*, vol. 27, no. 8, p. 084101, Jul. 2018.

[25] S. M. Mohammadi *et al.*, "Orbital angular momentum in radio—A system study," *IEEE Trans. Antennas Propag.*, vol. 58, no. 2, pp. 565–572, Feb. 2010.

[26] W. Guo, G. Wang, H. Li, Y. Zhuang, and C. Shuai, "Ultra-thin reflecting polarization beam splitter under spherical waves' illumination by using single-layered anisotropic metasurface," *Appl. Phys. A, Solids Surf.*, vol. 123, p. 103, Dec. 2017.

KAI-YUE LIU was born in China in 1993. She received the B.S. degree in computer science and technology and the M.S. degree in electromagnetic field and microwave technology from Air Force Engineering University, Xi'an, China, in 2014 and 2016, respectively, where she is currently pursuing the Ph.D. degree.

Her current research interests include metamaterials, metasurfaces, and their applications in novel antennas and multifunctional devices.

WEN-LONG GUO was born in China in 1993. He received the B.S. degree in radar engineering and the M.S. degree in electromagnetic field and microwave technology from Air Force Engineering University, Xi'an, China, in 2014 and 2016, respectively, where he is currently pursuing the Ph.D. degree.

His current research interests include metamaterials and their applications for performance enhancement of novel antennas.

GUANG-MING WANG was born in China in 1964. He received the B.S. and M.S. degrees from Air Force Engineering University, Xi'an, China, in 1982 and 1990, respectively, and the Ph.D. degree from the University of Electronic Science and Technology, Chengdu, China, in 1994, all in electromagnetic field and microwave technology.

He joined Air Force Engineering University as an Associate Professor, was promoted to Full Professor in 2000, and is currently the Head of the Microwave Laboratory. He has authored and co-authored over 100 conference and journal papers. His current interests include microwave circuits, antennas, and also the new structures, including EBG, PBG, metamaterials, fractals, and so on.

Dr. Wang has been a Senior Member of the Chinese Commission of Communication and Electronic. Since 1994, he has been awarded and warranted several items supported under the National Natural Science Foundation of China and fulfilled many local scientific research programs.

HAI-PENG LI was born in China in 1991. He received the B.S. and M.S. degrees in electromagnetic field and microwave technology from Air Force Engineering University, Xi'an, China, in 2013 and 2015, respectively.

His research interests include metamaterials, metasurfaces, and their applications to novel antennas and multifunctional devices. He has published over 10 peer-reviewed first-author papers in the IEEE Transaction on Antennas and Propagations,the IEEE Antennas and Wireless Propagation Letters, *Progress in Electromagnetic Research,* and so on.

GANG LIU was born in China in 1964. He received the B.S. degree in electromagnetic field and microwave technology from Xidian University, Xi'an, China, and the M.S. degree in electromagnetic field and microwave technology from Northwestern Polytechnical University, Xi'an, in 1987 and 1998, respectively.

His research interests include novel antenna and electromagnetic compatibility.